Transactions on Additive Manufacturing Meets Medicine
Trans. AMMM, 2025, Vol. 7, No 1, Article ID 2086, 10 Pages

Infinite Science Publishing

Original Research Article

Design and analysis of mechanical and permeability properties of stochastic scaffolds for biomedical applications

M. Khalil[1], G. Choi[1], P. P. Conway[1] and C. Torres-Sanchez[1*]

[1] *Multifunctional Materials Manufacturing Lab, Wolfson School, Loughborough University, Leics LE11 3TU, UK*
[*] *Corresponding author, email: c.torres@lboro.ac.uk*

Abstract: Bioengineered scaffolds with optimized osteoconductive and osteoinductive properties are highly desirable in bone tissue regeneration. Stochastic porous structures, resembling human trabecular bones, have gained increasing attention due to their suitability and superior performance in bone healing compared to regular porous architectures. In this study, we designed six trabecular-like porous scaffolds with varying porosity and surface area-to-volume ratios. The scaffolds were fabricated using pure titanium via selective laser melting, and their morphological characteristics were analyzed via micro computed tomography. Quasi-static compression testing was conducted to assess mechanical properties. The results showed that the as-built scaffolds exhibited a porosity range 67–71%, an average pore diameter ranging 440–565 µm, a quasi-elastic gradient between 2.6–3.5 GPa, and a yield strength of 44–58 MPa. These values closely match those of the cortical bone, indicating potential for orthopedic applications by mitigating stress shielding and enhancing implant longevity. Additionally, the permeability and wall shear stress were measured to predict cell growth performance in the scaffolds. The as-built models have a satisfactory permeability range of 6×10^{-9} to 15×10^{-9} m^2, which is higher than that of cancellous bone, benefitting prospects for nutrient flow and by-product removal that encourage osteoblastic mineralization.

I. Introduction

The optimum scaffold for bone tissue restoration should be structurally and mechanically similar to natural bone; not only the materials chemistry but also the three-dimensional (3D) porosity structure are regarded as critical for bone regeneration [1]. Some reports suggest that the optimum bone tissue engineering scaffold has macro-pores of size larger than 300 µm and porosity larger than 50% [2]. Another significant feature of the tissue engineering embodiment is the high surface area-to-volume (S/V) ratio requirement for scaffold-cell interaction and implant-bone attachment [3]. Previous research has demonstrated that scaffolds with trabecular bone structures built using computed tomography are biocompatible. However, reverse modelling scaffolds lack design flexibility, restricting their customization for specific therapeutic applications [4], [5].

Over the decades, porous structure design has shifted from irregular to regular and back to irregular. Before the advent of 3D printing, titanium implants relied on pore-forming agents to achieve porosity, with structure dictated by process parameters [6]. With 3D printing, researchers can now directly design and control implant porosity [7]. Selective laser melting (SLM), a popular additive manufacturing technology, has the potential to create 3D complex architecture with customized pores. What is more essential, SLM can print with commercially pure titanium (cp-Ti) powder and can manufacture more sophisticated implants with tailored architectures and inertness [8].

Stochastic Voronoi-based lattice structures show great potential for bone regeneration in tissue engineering, as they closely mimic the interconnectivity of natural bone [9]. These structures have been found to enhance cell proliferation and differentiation, particularly in the middle and late stages of osteogenesis, compared to regular scaffolds. The irregular porosity of trabecular scaffolds provides diverse local pore structures with variable curvature and pore sizes. While large curvature or small pores can hinder the diffusion of cytokines and growth factors, they also serve as anchor points for cell adhesion

Infinite Science Publishing

[10]. Additionally, Laing et al. [4] suggested that trabecular-like porous structures may outperform gradient regular porous scaffolds in promoting osteocyte differentiation due to their biomimetic architecture, which features a wide pore size distribution and varied shapes.

The random irregular structure of trabecular-like scaffolds enhances the diversification and generalization of physical effects, creating a varied mechanical stimulation environment that better aligns with the requirements for osteogenic stimulation [10]. Currently, Voronoi-based irregular porous structures are constrained by specific modeling methods, making precise morphological control challenging. Additionally, the relationship between design parameters, manufacturing method, and morphological and mechanical properties remain unclear due to absence of physical validation data in some studies [9], [11].

Flow-through dynamics should be addressed in tandem with mechanical properties. Permeability of the scaffold must be evaluated as this impacts cell metabolism. Permeability is defined as the ability of the porous media to allow fluid to pass through, and it can determine the nutrition available for cell differentiation and proliferation. According to Darcy's law [12], permeability's validity depends on the flow characteristics quantified by Reynolds number, which should be < 10, and this has typically informed flow rates that evaluate permeability and its effect on cellular behaviour. In addition to permeability, the flow-induced wall shear stress (WSS) is significant for cell growth [13]–[15]. Magnitudes of WSS inform about how cells can attach to the wall surface and survive. If the WSS is too high, cells may fail to survive within the fluid dynamics. In addition to the magnitude of the WSS, its uniformity is also critical for cell growth; a more homogeneous WSS distribution is preferred.

This study aimed to explore the relationship between the structural characteristics (porosity, pore size, and S/V ratio) of stochastic structures and their mechanical strength and permeability. We employed a design strategy for constructing structures within a targeted porosity and S/V ranges and examined the impact of SLM manufacturing limitations on the morphological, load-bearing capacity and permeability of as-built cp-Ti structures. Our findings offer insights into their application as orthopedic implants.

II. Material and methods

II.I. Lattice design and manufacturing

Six strut-based lattices were designed using nTop (v.4.6.2, nTopology Inc., USA). Seed points were randomly distributed within a 1 cm³ design space using 0.9-1.7 mm point spacing values. The volume was then partitioned into cells using the Voronoi tessellation method [16]. The strut thickness values (t) of 0.2-0.6 mm were applied to the edges, resulting in a scaffold composed of circular struts. The selection of point spacing and strut thickness values aimed to achieve a target porosity of 75-85% and a surface area-to-volume ratio (S/V) between 20 to 30 cm⁻¹. All scaffolds were created with a random seed value of 1.

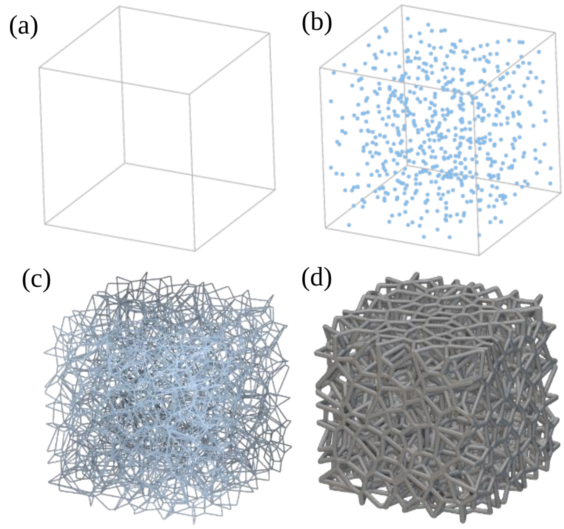

Figure 1: Stages of scaffold design creating an (a) design space of 10x10x10 mm³, (b) points map generated based on the point spacing value, (c) graph of Voronoi cells and (d) scaffold body by applying the strut thickness.

Table 1: Design parameters for the scaffolds.

Scaffold ID	Point Spacing (mm)	Strut Thickness (mm)	Porosity (%)	S/V (cm^{-1})
T2115	1.15	0.2	84.98	26.76
T2110	1.1	0.2	83.85	28.65
T3140	1.4	0.3	78.98	24.78
T3130	1.3	0.3	75.84	27.67
T4170	1.7	0.4	75.96	21.48
T4165	1.65	0.4	75.00	22.1

The build preparation was done using Materialise Magics v22.01 (Materialise, Belgium), and the samples were positioned on the build plate standing on 0.4 mm diameter stilts spaced approximately 2 mm to help heat dissipation. They were fabricated with a Trumpf TruPrint 1000 SLM printer (Trumpf, Ditzingen, Germany) using grade 1 cp-Ti powder (d10 = 20 µm, d50 = 34 µm, d90 = 45 µm) produced via gas atomization (AP&C, Boisbriand, Canada). Printing was performed with a single border and a zigzag infill strategy rotated 90° with each layer of 20 µm thickness. A laser power of 123 W was employed for contours and hatches with a laser speed of 1013 mm/s. The samples were cut off from the build plate using a high-speed saw (Buehler, USA) and cleaned in an ultrasonic bath (Grant Instruments, UK) with distilled water for 30 minutes to remove any loose powder. No further treatment was applied.

II.II. Morphological characterization

The open porosity (φ) of the manufactured scaffolds was determined using a two-step method. First, the material's bulk density ($\rho_{material}$) was measured following Archimedes' method (ASTM D792-20 standard). The sample was first weighed dry (m_{dry}) and then submerged in acetone, where its submerged weight (m_{sub}) was recorded. The acetone temperature was monitored during the process to ensure accurate density selection ($\rho_{acetone}$). The bulk density was then calculated using Eq. 1.

$$\rho_{material} = \frac{\rho_{acetone} \times m_{dry}}{m_{dry} - m_{sub}} \quad (1)$$

Subsequently, the open porosity of the samples was calculated using Eq. 2, where V_b represents the bulk volume of the scaffold.

$$\varphi\ (\%) = \left(1 - \frac{m_{dry}}{\rho_{material} \times V_b}\right) \times 100 \quad (2)$$

The as-built lattices were scanned using a v|tome|x M (Waygate Technologies, Pennsylvania, USA) micro computed tomography (µCT) system with an X-ray voltage of 180 kV, 50 µA current, and 10 µm scan resolution in XYZ, using a 0.5 mm Cu filter. Data was exported as a 16-bit 3D volume and analyzed in ORS-Dragonfly v.2022.2 (Comet Technologies, Montréal, Canada). Images were filtered and segmented into solid and void phases. The volume of the solid phase was used to calculate the open porosity and S/V ratio of the lattices. The voxel data of the solid phase was then tessellated into a surface mesh (STL) to be used for meshless simulation.

II.III. Mechanical characterization

The mechanical properties of the designed structures were estimated in nTop using linear static structural analysis. A representative volume element (RVE) of 5 × 5 × 5 mm was used to determine the effective elastic modulus (E) of the whole structure. For boundary conditions (BC), the top nodes of the model were displaced by 0.02 mm in the -Z direction, while all degrees of freedom, except for displacements normal to the load, were constrained. The bottom nodes were fully restrained in all directions. The sum of reaction forces on the bottom plates was used to calculate the applied stress by dividing it by the model's cross-sectional area. The elastic modulus (E) was then determined from the computed stress and strain values.

To ensure accuracy, a mesh sensitivity analysis was conducted on variant T2110, which featured the highest number of struts with the thinnest diameter. The details of the elements with converged E and the corresponding simulation times are presented in Table 2. The mesh element size ranged 0.2-0.04 mm and values of E converged at mesh element size of 0.06 mm. This did not rise further noticeably for smaller mesh size. Hence, 0.06 mm mesh size was used for finite element analysis (FEA) of all variants.

Table 2: Mesh sensitivity analysis results of T2110 lattice.

Mesh size (mm)	Number of elements	E (GPa)	Discrepancy (%)	CPU time (sec)
0.2	313,053	1.797	0.00	65
0.12	594,593	1.859	1.97	95
0.06	1,883,812	1.891	0.12	406
0.04	3,332,744	1.891	0.03	492

Monotonic compression testing was performed on the as-built samples using a UTM (Instron 3369, UK) with a 50 kN load cell (BS ISO 13314). A constant displacement rate of 0.01 mm/s was applied, with platen displacement recorded using an linear variable differential transformer (LVDT) (±6.25 µm accuracy). Samples (n = 3) were preloaded to 5 N and compressed to 30% of their gauge height. Stress-strain curves from raw UTM data permitted quasi-elastic gradient evaluation from the elastic region's slope, and yield strength was calculated using the 0.2% strain offset method. The first peak on the curve was recorded as the first maximum compressive strength.

Using µ-CT scan data, an image-based simulation method was employed to determine the compressive properties of the as-built structures. SimSolid 2023 (Altair Engineering Inc., Michigan, USA), a meshless simulation tool, was used for this purpose. The 5 × 5 × 5 mm RVE as-built structure was compressed between two rigid plates, with the bottom plate fully constrained while the top plate was displaced by 0.2 mm along the -Z axis, with all other degrees of freedom restricted. Separating contact conditions were applied at the interface between the lattice and rigid plates, with a friction coefficient of 0.3. Similar to FEA, the total reaction forces on the bottom plate were used to determine E.

II.IV. Numerical methods in CFD

In addition to the compression test, we conducted computational fluid dynamics (CFD) to analyse flow dynamics through the scaffolds and estimate their permeability (COMSOL Multiphysics v6.2, Stockholm, Sweden). The following governing equations for steady-state, incompressible, and Newtonian single-phase flow in three-dimensional domain are calculated:

$$\Delta \cdot \mathbf{u} = 0, \quad (3)$$

$$\rho \mathbf{u} \cdot \nabla \mathbf{u} = -\nabla p + \mu \nabla^2 \mathbf{u}, \quad (4)$$

where u is the velocity vector, ρ is the fluid density, µ is the fluid viscosity, and p is the pressure. A density of 1000 kg·m^{-3} and a viscosity of 0.001 Pa·s were used, and the gravity was neglected [17]–[19].

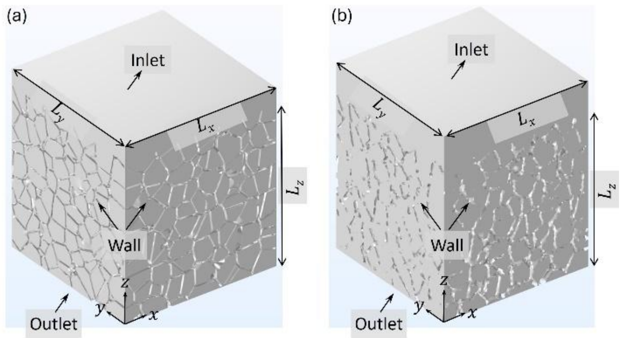

Figure 2: Schematic of computational fluid domains for (a) as-designed and (b) as-built models.

The computational domains with boundary conditions for as-designed models (Fig. 2a) and as-built models (Fig. 2b) depict the identical lengths of L_x, L_y, and L_z: 9.9 mm for as-designed T2110 and T2115, 9.88 mm for as-designed T3130 and T3140, and 9.8 mm for as-designed T4165 and T4170. For the as-built models, a length of 9.9 mm is used for T2110 and T2115, while a length of 9.8 mm is used for the others.

A dummy domain is introduced at the inlet to prevent any disturbance to the inlet boundary condition, where a mass flow rate of 11 ml/min is applied. Here, the flow rate is determined under the assumption that Darcy's law is valid for Reynolds number up to 10. We manually set an average flow rate of 11 ml/min to ensure a Reynolds number of 1 across all scaffolds.

A zero-pressure outlet boundary condition is imposed on the bottom surface, while no-slip wall boundary conditions are applied to the remaining surfaces. We generated the mesh using Altair HyperMesh 2024 and determined the optimal number of elements to range from 12 to 15 million for the as-designed and from 36 to 45 million for the as-built models, ensuring a balance between accuracy and computational efficiency.

III. Results and discussion

III.I. Lattice design

The goal was to design structures with a target porosity of 75–85% and an S/V ratio of 20–30 cm^{-1}. This range was selected based on our previous studies [2][20], where the as-built samples showed a 15% porosity reduction and a 25% increase in S/V ratio due to SLM manufacturing limitations. Accordingly, we anticipated that the actual porosity of the structures included in this study would exceed 70%, with an S/V ratio of 25–35 cm^{-1}.

Within the provided design space, three key variables for lattice generation were manipulated: random seed value, point spacing, and strut thickness. Initial testing showed that the random seed value was a minor factor, whereas strut thickness and point spacing significantly influenced the structures' physical properties.

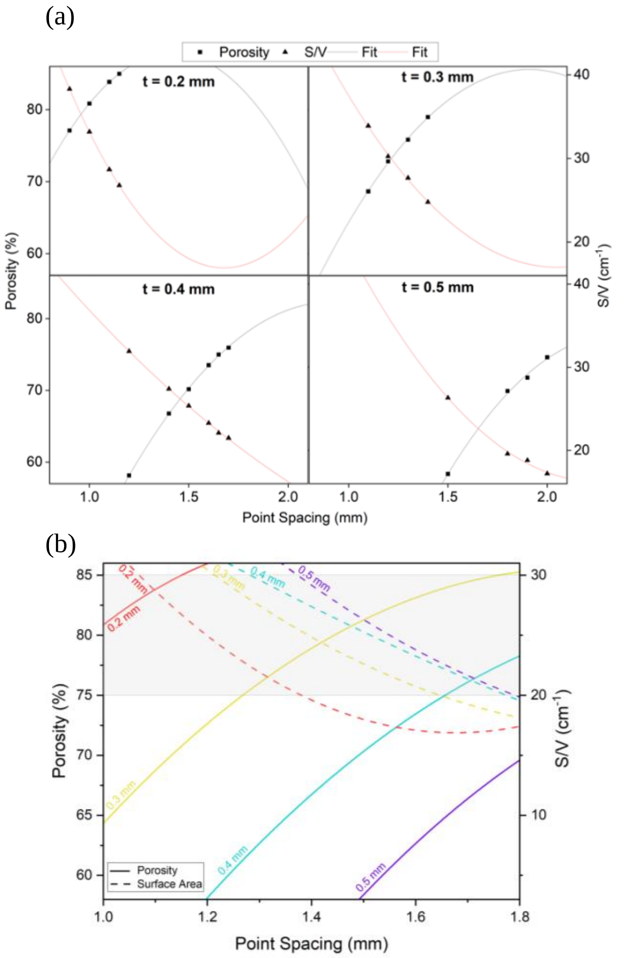

Figure 3: Relationship of strut thickness and point spacing for lattice design.

By selecting a strut thickness value, different designs were generated by varying point spacing. Since the minimum feature size strongly depends upon the beam spot size [21], [22], which in our case is 55 µm, a minimum strut thickness of 0.2 mm was considered as a starting point. Thickness values in the increment of 100 µm were tested up to 0.5 mm (Fig. 3a), revealing that only the 0.2–0.4 mm range met the target porosity and S/V ratio criteria (Fig. 3b).

III.II. Porosity and microstructure

The main morphological parameters of the as-built samples, porosity, S/V, strut thickness and pore sizes, were measured from µ-CT scan data. The values (As-B) are compared with the intended values (As-D) in Table 3.

Table 3(a): Designed (As-D) vs built (As-B) porosity and S/V.

Scaffold ID	Porosity (%)		S/V (cm^{-1})	
	As-D	As-B a)	As-D	As-B b)
T2115	84.99	70.32	26.5	33.41
T2110	83.60	67.61	28.7	35.16
T3140	79.46	70.81	23.6	28.00
T3130	76.73	67.23	26.0	30.95
T4170	76.34	71.00	20.1	23.27
T4165	75.01	68.88	21.0	24.47

Table 3(b): Comparison of strut thickness and pore sizes (As-D vs As-B).

Scaffold ID	Strut thickness (µm)		Pore size (µm)	
	As-D	As-B [b)]	As-D	As-B [b)]
T2115	224±4	281±37	558±191	458±164
T2110	224±4	286±39	534±179	440±157
T3140	320±4	325±39	605±223	507±205
T3130	321±4	328±40	561±201	471±189
T4170	417±6	388±48	669±261	565±246
T4165	417±6	390±49	651±249	547±234

[a)] Measurements as per ASTM D792-20 standard (n=1);
[b)] Measurements by µCT data analysis. Median±MAD values aregiven for strut thickness and pore size.

These stochastic lattice designs consist of numerous struts distributed randomly across the structure at varying angles and nodal connectivity. Unlike sheet-based Triply Periodic Minimal Surfaces (TPMS), which benefit from better manufacturability due to their continuously varying wall inclination angles [23], stochastic lattices are more susceptible to SLM limitations, particularly in supporting horizontal and near-horizontal struts. This leads to deviations in the morphological properties of the as-built structures compared to the as-designed, as evident in Table 3(a-b). The morphological properties of as-built structures are plotted against the as-designed values in Fig. 4 for each of the three strut thicknesses (t).

Notably, the designed strut thickness values in Table 3 and Fig. 4 appear slightly higher than those used in the initial design models (Table 1). This discrepancy arises because the thickness of the design model is measured using the Dragonfly's sphere-fitting method [24], the same method applied for evaluating the thickness of the actual samples.

Variants with 0.2 mm strut thickness (T2110 and T2115) exhibited the greatest deviations in porosity, thickness, pore size, and S/V ratio from the design specifications (Fig. 4). Among these, strut thickness showed the most significant variation, with T2110 struts being +28% thicker, whereas T4165 had a relatively small deviation of -6.3% showing thinning of the struts. The S/V ratio was the second most affected parameter (20–28% deviation), followed by pore size and porosity which were both reduced. Despite the reduced median thickness values of T4165 and T4170 scaffolds, the porosity was reduced by only 6% and 5.3% respectively. This is explained by significantly larger median absolute deviation (MAD) of as-built thickness values compared to intended values.

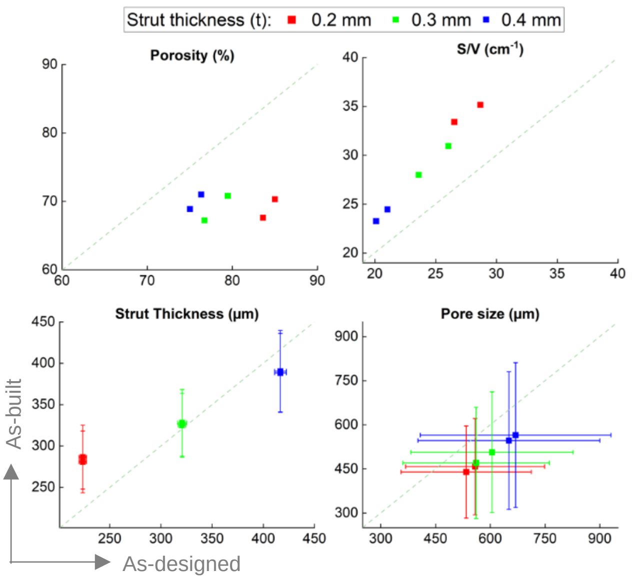

Figure 4: Percentage deviations values of as-built morphological properties against as-designed plotted with the intended thickness.

The primary reason for these deviations is the size-dependent thermal behavior inherent to the SLM process; thinner struts retain more heat, as their limited cross-section restricts effective heat dissipation into the lattice structure. Instead, more heat is absorbed by the adjacent powder, enlarging the melt pool and leading to increased strut thickness while reducing the open porosity [4].

An increase in average strut thickness in SLM as-built samples has been reported [2], [4], [25], with smaller strut diameters exhibiting higher deviations from the design thickness [4]. Similarly, reductions in porosity [2], [4], [26], [27] and pore size [2], [25], [27] have been observed in similar irregular samples.

S/V values, largely overlooked in lattice design and rarely reported, generally increase due to the contribution of semi-sintered particles adhered to the struts [2]. However, a few studies [4], [27] have reported S/V value reductions despite increased strut thickness and reduced porosity. This has been attributed to the presence of small, slender pores, the absence of sharp corners, and a significant increase in the overall volume of the as-built lattice.

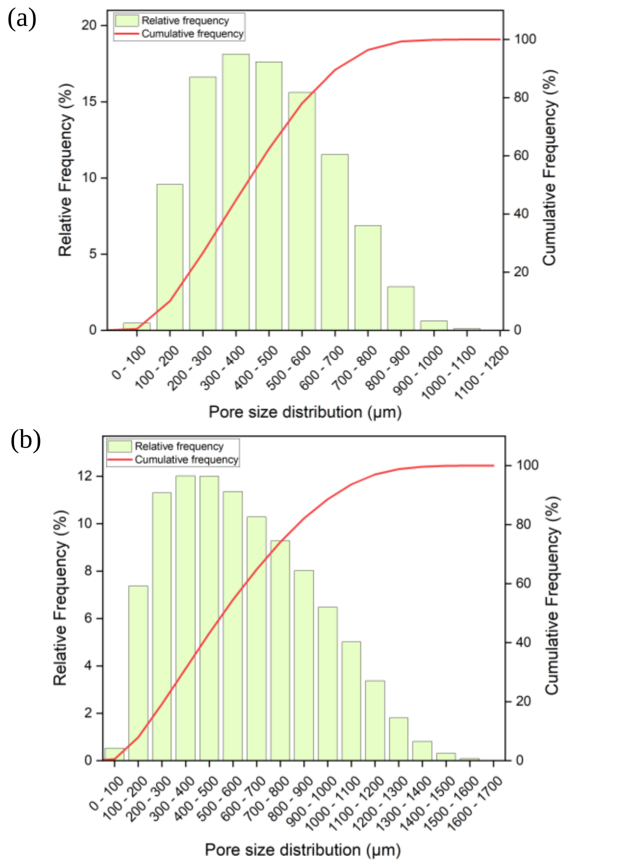

Figure 5: Pore size distribution in as-built T2110 (a) and T4170 (b) variants.

The pore size distribution plots (Fig. 5) for the T2110 and T4170 lattices reveal the presence of a wide range of pore sizes in these structures. T2110, with a median pore size of 440 µm, contains pores as large as 1200 µm in diameter. In the case of T4170, the pore size extends up to 1700 µm. A significant proportion of these pores exceed 300 µm, the recommended minimum pore size for bone tissue engineering [2]. Additionally, the distribution data, particularly for T4170, is positively skewed rather than normally distributed. Therefore, median and MAD values are reported in this study, as they better represent the population than the mean and standard deviation.

The deviation in the morphological properties of the as-built structures compared to the as-designed counterparts can be minimized through post-processing which not only could help bridge the gap between them, but would also remove loosely attached surface particles which are a risk to the body if they were to detach after implantation [28].

III.III. Mechanical properties

The monotonic stress-strain curves from quasi-static compression testing (Fig. 6a) display a similar behavior amongst all variants because their porosity values fall within a narrow range (67–71%). A distinct first peak stress (first maximum strength) is observed in all cases. Following this peak, the stress value drops and plateaus roughly between 15–25% strain before rising again (densification), in a stretch-dominated behavior [22].

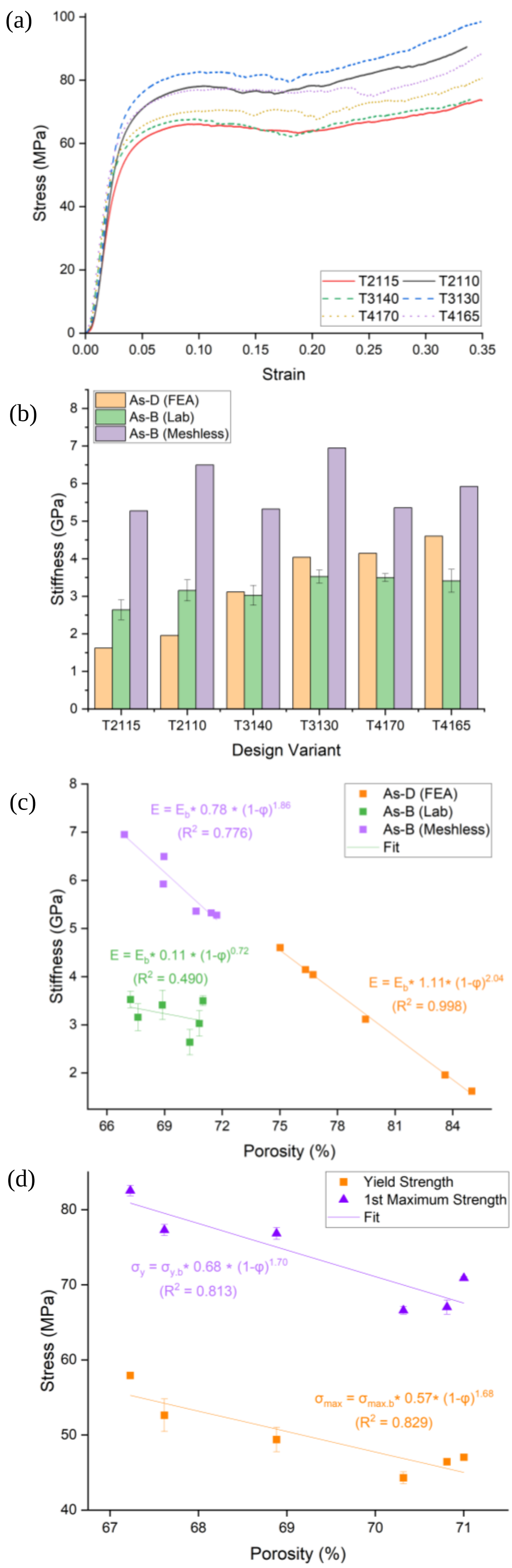

Figure 6: (a) Stress-strain curves of all specimens; (b) Effective modulus comparison:as-designed vs as-built determined by FEA, lab testing and meshless method; (c, d) Modulus/yield/1st max strength vs porosity for as-designed and as-built samples.

The quasi-elastic gradient values obtained from stress-strain curves were compared with the FEA results from the as-designed CAD models (Fig. 6b). For the T2110 and T2115 variants, the modulus estimated by FEA is < 2 GPa, making it the least stiff structure amongst all. The stiffest response was expected from T4165 (lowest porosity in the batch).

Due to the actual porosities of the structures being lower than as-designed (see III.II section), deviations in mechanical properties compared to FEA estimates were anticipated. Variants with a 0.2 mm strut thickness (i.e. T2X) exhibited higher stiffness in lab testing than in FEA, which can be attributed to their largest deviation in porosity among all samples. The difference between FEA and lab testing results was minimal for the middle strut thickness designs, while the stiffness of the remaining structures was found to be lower than the FEA estimate.

To analyze the relationship between quasi-elastic modulus, yield strength, and first maximum strength and porosities, the Ashby-Gibson fitting was applied using Eqs. 5 and 6.

$$E = E_b * C * (1 - \varphi)^n \tag{5}$$

$$\sigma = \sigma_b * C * (1 - \varphi)^n \tag{6}$$

Where E_b and σ_b represent the modulus of elasticity and yield/ultimate strength of the bulk material, and C and n are empirically determined coefficients.

A linear relationship between stiffness (effective modulus) and porosity confirms the Ashby-Gibson theory (eq. 5, Fig. 6c). The FEA results show a strong correlation with porosity, whereas the lab results exhibit significant scatter with a low regression value. The coefficient C was 1.11 for FEA and 0.11 for lab testing, while the coefficient n was 2.01 and 0.72, respectively.

The coefficient values from FEA simulations suggest a bending-dominated behavior in these structures, whereas the lab results indicate stretching-dominated characteristics [29]. Yield and first maximum strengths obtained from the lab tests on the as-built samples also correlated with porosity (eq. 6), however with low regression values (Fig. 6d).

To confirm this, the stiffness values of the as-built samples were also determined using image-based simulation via a meshless method. When compared to the lab-tested values, meshless simulation results were found to be significantly higher (Fig. 6B). These values were plotted against the porosities (Fig. 6C) and a better linear relationship was found between them compared to the lab test results. The values of both Ashby-Gibson coefficients were found also closer to the FEA results. This indicates mechanical underperformance in the lab testing of the as-built samples at their porosity level.

Since only monotonic compression testing was performed on the specimens, the quasi-elastic gradient was calculated from the slope of the first loading cycle. In uniaxial compression testing, the slope of the first loading cycle is lower than that of the unloading curve due to localized plasticity well below the compressive strength of metallic foams [30].

To achieve more stabilized mechanical behavior, loading-unloading cycles are typically performed to determine the elastic gradient of the structures [29]. Various studies comparing monotonic and cyclic loading tests have found a significant increase (up to 2.4 times) in the stiffness of porous structures after the first loading due to strain hardening [29], [31], [32]. This explains the discrepancy between the results of image-based simulations and lab testing. With cyclic loading, these discrepancies can be reduced in these stochastic structures, and this is the matter of further investigations.

Nevertheless, when compared to human trabecular bone which has elastic modulus and compressive strength in the ranges of 1.5-11.2 GPa and 11-24 MPa respectively [33], the stiffness values of these lattice specimens lie within the target ranges with their yield strength surpassing it. This means that these structures can provide sufficient mechanical support while reducing stress shielding and maintaining a significant safety factor away from permanent deformation.

III.IV. Permeability tests

To predict scaffolds' performance in terms of cellular behaviour, we estimated their permeability and WSS. The permeability (k), which is derived from Darcy's law, and WSS are calculated as follows:

$$k = \frac{Q\mu L}{A\Delta p}, \tag{7}$$

$$\mathrm{WSS} = \mu \frac{\partial \mathbf{u}}{\partial n}, \tag{8}$$

Where Q is the flow rate, L is the length of the scaffold along the flow direction, A is the surface area, Δp is the pressure drop, and n is the normal vector to the wall surface.

Fig. 7 shows the cross-sectional velocity contour at the centre along the x-axis for the as-designed (Fig. 7a) and as-built (Fig. 7b) T2110 scaffold, an exemplar of the set.

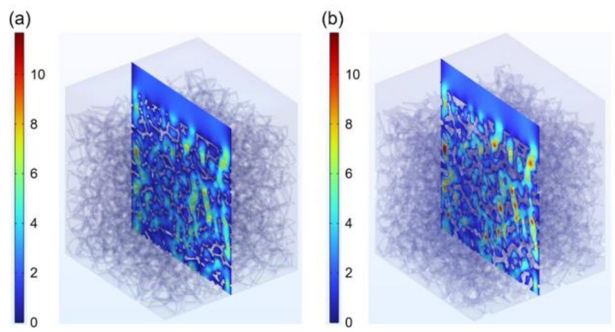

Figure 7: Velocity magnitude (mm/s) contour at the cross-sectional center along the x-direction for (a) the as-designed and (b) the as-built model of T2110.

Infinite Science Publishing

The maximum velocity magnitude of the as-built model is higher than that of the as-designed. As discussed earlier, the as-built scaffold has lower porosity, resulting in a reduced cross-sectional area for fluid flow. Consequently, the velocity increases overall and some regions with higher roughness can further contribute to a higher velocity. In addition to velocity magnitude, the pressure contour for the as-designed (Fig. 8a) and as-built (Fig. 8b) models are depicted. The pressure in the as-built model is higher than that in the as-designed model, indicating greater resistance to fluid flow. Since permeability is defined by Eq. 7, the permeability of the as-built model is higher than that of the as-designed model. The other scaffolds follow the same trend when comparing the as-designed and as-built models.

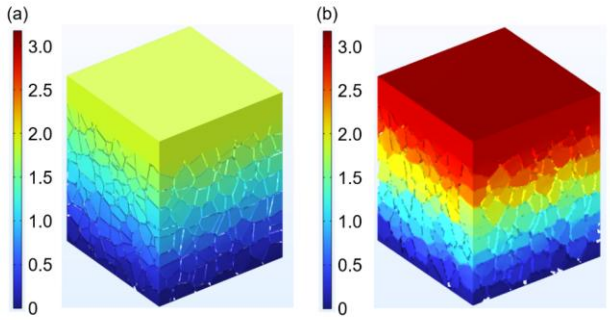

Figure 8: Pressure (Pa) contour of (a) the as-designed and (b) as-built T2110 models.

To gain a deeper understanding of the discrepancies between the as-designed and as-built models, we quantified their permeability and compared the results (Fig. 9a). The permeability for all models is higher than that of cancellous bone (5×10^{-9} m^2 [17], [34], [35]), meeting the requirement for scaffold design. It is noteworthy that T4170 exhibits the highest permeability despite not having the highest porosity. This means the permeability depends not only on the porosity but also on other factors, such as tortuosity, roughness, etc.

However, when comparing models with the same strut thickness, a model with higher porosity exhibits higher permeability. For example, T4170 has higher permeability than T4165.

For all designs, the as-designed models have higher permeability than the as-built models, as expected, due to the decrease in porosity and the increase in roughness. The discrepancy in permeability between the as-designed and as-built models varies significantly depending on the difference in porosity. For example, the discrepancy for T4165 and T4170 is smaller than for the other models, as the difference in porosity is lower. For the as-designed models, T2110 has higher permeability than T3130. However, for as-built models, T2110 has a lower permeability than T3130 (Fig. 9a). This is due to the greater loss of actual porosity for T2110.

In addition to permeability, we measured the surface-averaged WSS (Fig. 9b). The as-designed models have lower surface-averaged WSS than the as-built models for all designs, consistent with the trend observed in permeability. T4170 has the lowest surface-averaged WSS, which aligns well with its highest permeability.

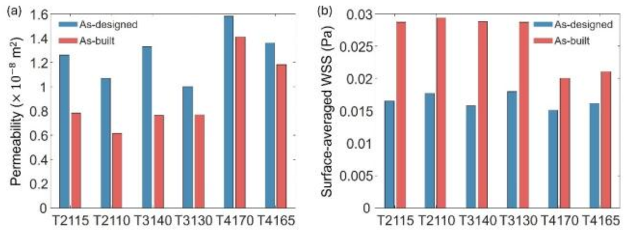

Figure 9: Comparison of the as-designed (blue) and as-built (red) models for (a) permeability and (b) surface-averaged WSS.

This indicates that surface-averaged WSS depends not only on porosity but also on other factors, as permeability does. The discrepancy in surface-averaged WSS between the as-designed and as-built T4165 and T4170 is lower than the other models, similar to the trend observed in permeability.

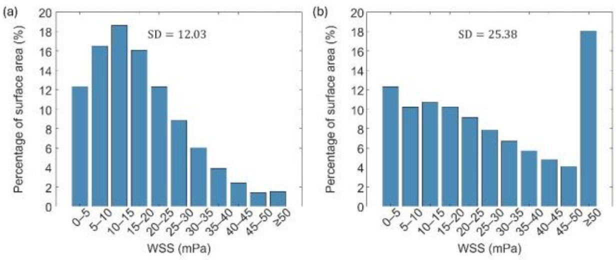

Figure 10: WSS distribution of (a) the as-designed and (b) as-built T2110 models with their standard deviation (SD).

To determine if a design satisfies the requirements of bone tissue scaffold in terms of cellular proliferation, differentiation and maturation, the WSS distribution should be evaluated. Fig. 10 illustrates WSS distribution for the as-designed (Fig. 10a) and as-built (Fig. 10b) T2110.

The WSS distribution of the as-designed model is more gaussian than that of the as-built model. The standard deviation of the as-built model (25.38) is twice as higher as that of the as-designed model (12.03), indicating a less uniform WSS distribution. This is potentially detrimental to cell growth [17], and maximum local values >56 mPa could lead to cell washout [36]. The full set of WSS distributions for as-built specimens is presented in Fig. 11.

The standard deviation of WSS is generally lower with larger point spacing for designs with same strut thickness. For example, T4165 has a higher standard deviation of WSS than T4170. Similarly, following the trend of the surface-averaged WSS, T4170 has a lower percentage surface area with WSS greater than 50 mPa.

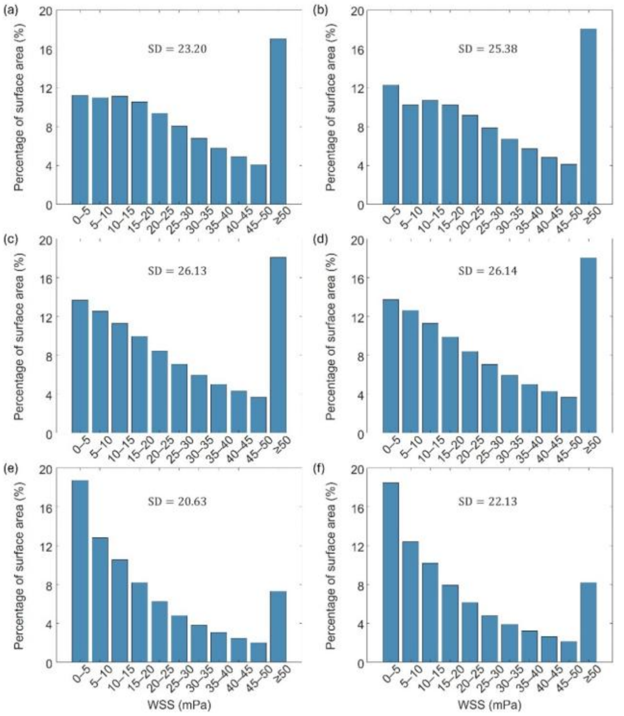

Figure 11: WSS distribution of the as-built (a) T2110, (b) T2115, (c) T3130, (d) T3140, (e) T4165, and (f) T4170 with their standard deviation (SD).

IV. Conclusions

In this study, we investigated the design, manufacture and validation of stochastic lattice structures with an intended range of porosity and S/V suitable for bone application, taking into account the manufacturing limitations of the SLM process. The mechanical behavior results of as-built structures were compared with mesh-based and meshless methods simulations. In addition to mechanical properties, we quantified permeability and WSS using CFD. The major findings of this study are summarized below.

The limitations of the SLM process have the greatest impact on lattice designs with smaller strut diameters, leading to significant deviations in strut thickness, surface-to-volume (S/V) ratio, and porosity compared to the intended values. This restricts the ability to manufacture scaffolds with high porosity while maintaining suitable S/V ratios.

The results demonstrate that porosity significantly influences the effective modulus and overall mechanical response of these structures. The discrepancy between FEA and lab results suggests that localized plasticity in the as-built samples during monotonic testing contributes to the actual mechanical performance of the structures. Furthermore, coefficient values derived from the Ashby-Gibson model indicate that FEA simulations predict bending-dominated behavior, whereas lab results suggest a more stretch-dominated response.

In addition, this study underscores the need for incorporating cyclic mechanical loading experiments to better capture the stabilized compressive response of these structures and a more faithful comparison with simulated scenarios.

Along with the mechanical properties, increases in porosity deteriorate both permeability and WSS. Furthermore, we found that they are influenced also by other factors, such as tortuosity and roughness. While the as-designed models exhibit satisfactory WSS distribution, those of the as-built counterparts are distributed more heterogeneously, leading to skewed profiles that would need recovering via a post-processing step to optimize their performance when deployed for bioengineering applications supporting cellular metabolism.

Post-processing will smooth the rough surface resulting in enhanced porosity and reduced design versus built deviations, improving the predictions of morphological, features, mechanical properties and permeability on the as-built samples when studying the as-designed models.

Acknowledgments

This research work is supported by a Wolfson School PhD Scholarship and EPSRC (grant number EP/V007335/1).

Author's statement

Conflict of interest: Authors state no conflict of interest. Animal experiments are not part of this study.

References

[1] S. Wu, X. Liu, K. W. K. Yeung, C. Liu, and X. Yang, "Biomimetic porous scaffolds for bone tissue engineering," *Mater. Sci. Eng. R Reports*, vol. 80, pp. 1–36, 2014, doi: https://doi.org/10.1016/j.mser.2014.04.001.

[2] C. Torres-Sanchez *et al.*, "Comparison of Selective Laser Melted Commercially Pure Titanium Sheet-Based Triply Periodic Minimal Surfaces and Trabecular-Like Strut-Based Scaffolds for Tissue Engineering," *Adv. Eng. Mater.*, vol. 24, no. 1, Jan. 2022, doi: 10.1002/adem.202100527.

[3] F. A. Shah, P. Thomsen, and A. Palmquist, "Osseointegration and current interpretations of the bone-implant interface," *Acta Biomater.*, vol. 84, pp. 1–15, 2019, doi: https://doi.org/10.1016/j.actbio.2018.11.018.

[4] H. Liang *et al.*, "Trabecular-like Ti-6Al-4V scaffolds for orthopedic: fabrication by selective laser melting and in vitro biocompatibility," *J. Mater. Sci. Technol.*, vol. 35, no. 7, pp. 1284–1297, 2019, doi: 10.1016/j.jmst.2019.01.012.

[5] Y. Du *et al.*, "Design and statistical analysis of irregular porous scaffolds for orthopedic reconstruction based on voronoi tessellation and fabricated via selective laser melting (SLM)," *Mater. Chem. Phys.*, vol. 239, no. August 2019, pp. 1–9, 2020, doi: 10.1016/j.matchemphys.2019.121968.

[6] X. Pei *et al.*, "Ti6Al4V orthopedic implant with biomimetic heterogeneous structure via 3D printing for improving osteogenesis," *Mater. Des.*, vol. 221, p. 110964, 2022, doi: 10.1016/j.matdes.2022.110964.

[7] G. Zhang, J. Li, X. Zhou, Y. Zhou, J. Xie, and A. Huang, "Research on Design and Performance of High-Performance Porous Structure Based on 3D Printing Technology," *J. Mater. Eng. Perform.*, 2024, doi: 10.1007/s11665-024-09607-z.

[8] L.-C. Zhang and H. Attar, "Selective Laser Melting of Titanium Alloys and Titanium Matrix Composites for Biomedical Applications: A Review," *Adv. Eng. Mater.*, vol. 18, no. 4, pp. 463–475, Apr. 2016, doi: 10.1002/adem.201500419.

[9] M. Rezapourian and I. Hussainova, "Optimal mechanical properties of Hydroxyapatite gradient Voronoi porous scaffolds for bone applications — A numerical study," *J. Mech. Behav. Biomed. Mater.*, vol. 148, no. September, p. 106232, 2023, doi: 10.1016/j.jmbbm.2023.106232.

[10] H. Liang *et al.*, "Trabecular-like Ti–6Al–4V scaffold for bone repair: A diversified mechanical stimulation environment for bone regeneration," *Compos. Part B Eng.*, vol. 241, no. June, p. 110057, 2022, doi: 10.1016/j.compositesb.2022.110057.

[11] D. B. Alemayehu, M. Todoh, and S. J. Huang, "Advancing 3D Dental Implant Finite Element Analysis: Incorporating Biomimetic Trabecular Bone with Varied Pore Sizes in Voronoi Lattices," *J. Funct. Biomater.*, vol. 15, no. 4, 2024, doi: 10.3390/jfb15040094.

[12] S. Whitaker, "Flow in porous media I: A theoretical derivation of Darcy's law," *Transp. Porous Media*, vol. 1, no. 1, pp. 3–25, 1986, doi: 10.1007/BF01036523.

[13] Z. Xiong, L. Rouquier, X. Huang, E. Potier, M. Bensidhoum, and T. Hoc, "Porosity and surface curvature effects on the permeability and wall shear stress of trabecular bone: Guidelines for biomimetic scaffolds for bone repair," *Comput. Biol. Med.*, vol. 177, no. C, Jul. 2024, doi: 10.1016/j.compbiomed.2024.108630.

[14] J. Melke, F. Zhao, B. van Rietbergen, K. Ito, and S. Hofmann, "Localisation of mineralised tissue in a complex spinner flask environment correlates with predicted wall shear stress level localisation.," *Eur. Cell. Mater.*, vol. 36, pp. 57–68, Jul. 2018, doi: 10.22203/eCM.v036a05.

[15] L. Liu, W. Yuan, and J. Wang, "Mechanisms for osteogenic differentiation of human mesenchymal stem cells induced by fluid shear stress.," *Biomech. Model. Mechanobiol.*, vol. 9, no. 6, pp. 659–670, Dec. 2010, doi: 10.1007/s10237-010-0206-x.

[16] G. De Pasquale and D. Barra, "Voronoi lattice-based orthotics with modular stiffness for additive manufacturing," *Trans. Addit. Manuf. Meets Med.*, vol. 4, no. 1, pp. 668–668, 2022, doi: 10.18416/AMMM.2022.2209668.

[17] D. Ali and S. Sen, "Finite element analysis of mechanical behavior, permeability and fluid induced wall shear stress of high porosity scaffolds with gyroid and lattice-based architectures," *J. Mech. Behav. Biomed. Mater.*, vol. 75, pp. 262–270, 2017, doi: https://doi.org/10.1016/j.jmbbm.2017.07.035.

[18] P. Vossenberg, G. A. Higuera, G. van Straten, C. A. van Blitterswijk, and A. J. B. van Boxtel, "Darcian permeability constant as indicator for shear stresses in regular scaffold systems for tissue engineering," *Biomech. Model. Mechanobiol.*, vol. 8, no. 6, pp. 499–507, 2009, doi: 10.1007/s10237-009-0153-6.

[19] X. Xue, M. K. Patel, M. Kersaudy-Kerhoas, M. P. Y. Desmulliez, C. Bailey, and D. Topham, "Analysis of fluid separation in microfluidic T-channels," *Appl. Math. Model.*, vol. 36, no. 2, pp. 743–755, Feb. 2012, doi: 10.1016/j.apm.2011.07.009.

[20] M. Khalil, M. Burton, S. Hickinbotham, P. P. Conway, and C. Torres-sanchez, "Simulation and physical validation of metal triply periodic minimal surfaces-based scaffolds for bioengineering applications.," *Eng. Model. Anal. Simul.*, vol. 2, no. 1, pp. 1–14, 2025, doi: https://doi.org/10.59972/fn8161af.

[21] M. McGregor, S. Patel, S. McLachlin, and Mihaela Vlasea, "Architectural bone parameters and the relationship to titanium lattice design for powder bed fusion additive manufacturing," *Addit. Manuf.*, vol. 47, no. August, p. 102273, 2021, doi: 10.1016/j.addma.2021.102273.

[22] M. Araya, M. Jaskari, T. Rautio, T. Guillén, and A. Järvenpää, "Assessing the compressive and tensile properties of TPMS-Gyroid and stochastic Ti64 lattice structures: A study on laser powder bed fusion manufacturing for biomedical implants," *J. Sci. Adv. Mater. Devices*, vol. 9, no. 1, 2024, doi: 10.1016/j.jsamd.2023.100663.

[23] C. Yan, L. Hao, A. Hussein, P. Young, and D. Raymont, "Advanced lightweight 316L stainless steel cellular lattice structures fabricated via selective laser melting," *Mater. Des.*, vol. 55, pp. 533–541, 2014, doi: 10.1016/j.matdes.2013.10.027.

[24] T. Hildebrand and P. Rüegsegger, "A new method for the model-independent assessment of thickness in three-dimensional images," *J. Microsc.*, vol. 185, no. 1, pp. 67–75, 1997, doi: 10.1046/j.1365-2818.1997.1340694.x.

[25] Y. Wang, C. Ma, Y. Wu, D. Gao, Y. Meng, and H. Wang, "Comprehensive Evaluation of Biomechanical and Biological Properties of the Porous Irregular Scaffolds Based on Voronoi-tessellation," *J. Bionic Eng.*, 2024, doi: 10.1007/s42235-024-00630-3.

[26] Y. Du *et al.*, "Finite element analysis of mechanical behavior, permeability of irregular porous scaffolds and lattice-based porous scaffolds," *Mater. Res. Express*, vol. 6, no. 10, 2019, doi: 10.1088/2053-1591/ab3ac1.

[27] M. Fantini and M. Curto, "Interactive design and manufacturing of a Voronoi-based biomimetic bone scaffold for morphological characterization," *Int. J. Interact. Des. Manuf.*, vol. 12, no. 2, pp. 585–596, 2018, doi: 10.1007/s12008-017-0416-x.

[28] E. Pehlivan, J. Džugan, J. Fojt, R. Sedláček, S. Rzepa, and M. Daniel, "Post-processing treatment impact on mechanical properties of SLM deposited Ti-6Al-4 V porous structure for biomedical application," *Materials (Basel).*, vol. 13, no. 22, pp. 1–11, 2020, doi: 10.3390/ma13225167.

[29] M. Benedetti *et al.*, "Study of the Compression Behaviour of Ti6Al4V Trabecular Structures Produced by Additive Laser Manufacturing," *Euro PM 2019 Congr. Exhib.*, 2019.

[30] J. W. H. and H. N. G. W. M.F. Ashby, A.G. Evans, N.A. Fleck, L.J. Gibson, "Metal Foams : A Design Guide Metal Foams : A Design Guide," 1899.

[31] L. Emanuelli *et al.*, "Manufacturability of functionally graded porous β-Ti21S auxetic architected biomaterials produced by laser powder bed fusion: comparison between 2D and 3D metrological characterization," *Int. J. Bioprinting*, vol. X, no. 3D Printing of Advanced Biomedical Devices, 2023.

[32] L. Boniotti, S. Beretta, L. Patriarca, L. Rigoni, and S. Foletti, "Experimental and numerical investigation on compressive fatigue strength of lattice structures of AlSi7Mg manufactured by SLM," *Int. J. Fatigue*, vol. 128, no. December 2018, p. 105181, 2019, doi: 10.1016/j.ijfatigue.2019.06.041.

[33] C. Torres-Sanchez, F. R. A. Al Mushref, M. Norrito, K. Yendall, Y. Liu, and P. P. Conway, "The effect of pore size and porosity on mechanical properties and biological response of porous titanium scaffolds," *Mater. Sci. Eng. C*, vol. 77, pp. 219–228, 2017, doi: 10.1016/j.msec.2017.03.249.

[34] I. Ochoa, J. A. Sanz-Herrera, J. M. García-Aznar, M. Doblaré, D. M. Yunos, and A. R. Boccaccini, "Permeability evaluation of 45S5 Bioglass-based scaffolds for bone tissue engineering.," *J. Biomech.*, vol. 42, no. 3, pp. 257–260, Feb. 2009, doi: 10.1016/j.jbiomech.2008.10.030.

[35] S. S. Kohles, J. B. Roberts, M. L. Upton, C. G. Wilson, L. J. Bonassar, and A. L. Schlichting, "Direct perfusion measurements of cancellous bone anisotropic permeability," *J. Biomech.*, vol. 34, no. 9, pp. 1197–1202, 2001, doi: https://doi.org/10.1016/S0021-9290(01)00082-3.

[36] F. Maes, T. Claessens, M. Moesen, H. Van Oosterwyck, P. Van Ransbeeck, and P. Verdonck, "Computational models for wall shear stress estimation in scaffolds: A comparative study of two complete geometries," *J. Biomech.*, vol. 45, no. 9, pp. 1586–1592, 2012, doi: 10.1016/j.jbiomech.2012.04.015.